

www.acsaem.org Article

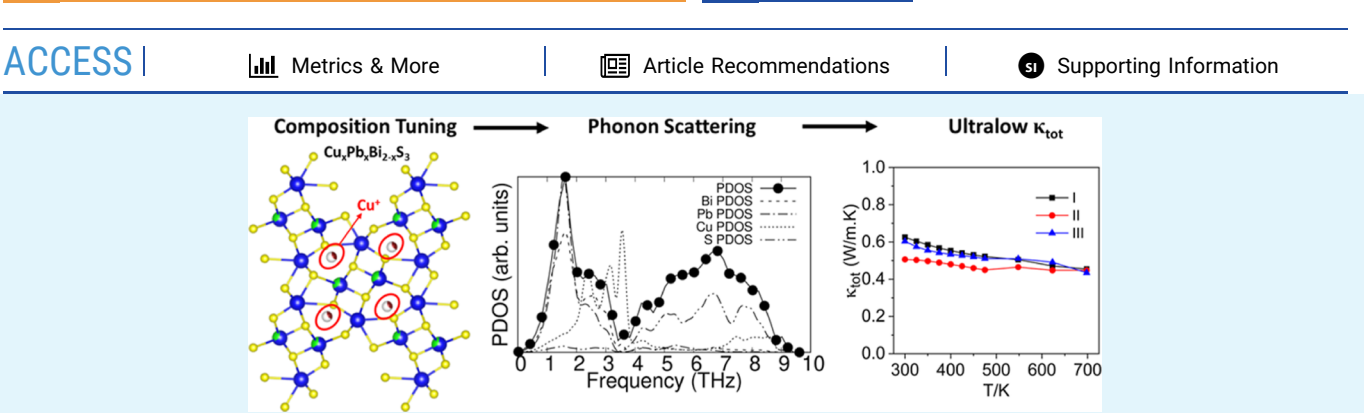
Ultralow Lattice Thermal Conductivity in the Aikinite Structure Family, $Cu_xPb_xBi_{2-x}S_3$, and Thermoelectric Properties of $Cu_{0.14}Pb_{0.14}Bi_{1.86}S_3$

Srikanth Balijapelly, Ashlee Hauble, Santhoshkumar Sundaramoorthy, Jeremy Lee Watts, Susan M. Kauzlarich, Aleksandr Chernatynskiy, and Amitava Choudhury*



Cite This: ACS Appl. Energy Mater. 2022, 5, 14222-14230





ABSTRACT: In this article, we report the synthesis, characterization, and ultralow thermal conductivity of three complex quaternary chalcogenide compounds, $Cu_xPb_xBi_{2-x}S_3$ [x=0.14(I), 0.33(II), and 1.0(III)], in the bismuthinite (Bi_2S_3)—aikinite ($CuPbBiS_3$) solid solution series. All the compounds in this solid solution series can be generated by progressively replacing Bi and a vacancy with Pb and Cu. Compositions in between the end members of the series possess complex disordered crystal structures with mixed occupied Bi/Pb and partially occupied Cu/vacancy sites. Density functional theory (DFT)-based phonon calculations suggest that these intrinsic structural attributes and presence of interstitial Cu lead to ultralow thermal conductivities less than 0.65 W m⁻¹ K⁻¹ between 300 and 700 K. All the compounds exhibit a narrow band gap below 1.0 eV confirmed by diffuse reflectance spectroscopy. DFT-based band structure analysis shows that the band gap decreases with the increasing amount of Cu and Pb substitution due to increased contribution of the Cu d states to the valence band. High-temperature charge transport properties indicate that electrons are the dominant charge carriers resulting in low electrical conductivities and relatively large Seebeck coefficients. A promising figure of merit, zT, of 0.21 for I has been achieved at 475 K.

KEYWORDS: thermoelectric, ultralow thermal conductivity, aikinite, complex chalcogenides, copper vacancy

INTRODUCTION

One of the key strategies to boost a material's thermoelectric performance is to minimize the total thermal conductivity (κ_{total}) as it resides in the denominator of the thermoelectric efficiency determination equation defined by the figure of merit, $zT = \frac{S^2 \sigma T}{\kappa_{\text{total}}}$, where S, σ , and T represent the Seebeck coefficient, electrical conductivity, and absolute temperature, respectively. 1-3 It is challenging to reduce the thermal conductivity without adversely affecting the electrical properties.^{3,4} However, it is possible to suppress the lattice thermal conductivity by introducing defects, grain boundaries, and nano-structuring, which are all in the hands of synthetic solid state chemists. In this scenario, it is also important to find materials with intrinsically low thermal conductivities with compositions that can be tuned to further improve the electrical properties. Not every family of compounds is bestowed with the freedom to create disorder or vacancies.

as it depends on the thermodynamic stabilities of both end members of the series. Hence, the doping strategy is limited to few specific dopants for which the coordination and bonding requirements must be satisfied. There exists a plethora of mineral compositions possessing complex crystal structures on which substitutional disorders and creation of vacancies are essential to tune the electronic and thermal components independently. For example, a homologous series of lillianite, cannizzarite, ^{5–7} and pavonite gives the freedom to tune the electrical properties as a function of slab thickness. ^{8–10}

Received: August 29, 2022 Accepted: October 20, 2022 Published: November 1, 2022





Recently, our group investigated Cu substitution in the makovickyite family of compounds and found that the lattice thermal conductivity can be suppressed by introducing Cu⁺ ions in the interstitial void spaces, which effectively scatter the phonons. All of these intrinsic assets make complex chalcogenide-based minerals a potential platform for tunable compositions.

Recently, working on a similar concept, we sought to synthesize a bismuthinite (Bi₂S₃)-aikinite (CuPbBiS₃) series of complex composition through progressive substitution of Bi with Pb and Cu, where Cu can take up the interstitial site. The systematic substitution of Pb and Cu for Bi generates several compositions $Cu_xPb_xBi_{1-x}S_3$ (x = 0 to 1) across the solid solution series with varied amounts of Cu and Pb for Bi. Many of these compositions especially from the naturally occurring minerals form ordered superstructures, for example, pekoite (CuPbBi₁S₁₈), ¹¹ gladite (CuPbBi₅S₉), ^{12,13} krupkaite (CuPbBi₃S₆), ¹² hammerite (Cu₂Pb₂Bi₄S₉), ¹⁴ or a new superstructure (Cu_{1.6}Pb_{1.6}Bi_{6.4}S₁₂). Some of these crystal structures are also interpreted as commensurately modulated structures by Petricek and Makovicky. On the other hand, aikinite (CuPbBiS₃, x = 1), 11,17,18 an end member of the series, is an ordered bismuthinite derivative generated by completely replacing one Bi and vacancy in Bi₂S₃ by Pb and Cu, respectively, where both Pb and Cu occupy ordered independent positions. There exists a range of compositions with 1 > x > 0 in the bismuthinite derivative, Cu_xPb_xBi_{1-x}S₃, having disorder between Cu and the vacancy and between Bi and Pb. 11 This solid solution series, which can also be called a Cu-deficient aikinite structure type, has structural complexity, compositional flexibility, and disorder, making it a potential thermoelectric material. However, not much work has been done in this direction. A reasonably good zT of 0.42 at 723 K has been reported for the gladite phase, CuPbBi₅S₉ (Cu_{0.33}Pb_{0.33}Bi_{1.66}S₃, x = 0.33), by Liang et al.¹⁹ They attributed the promising zT to low thermal conductivity resulting from low Debye temperature, low average velocity of sound, and large Grüneisen parameters. 19 While we were preparing our article, another extensive report on thermoelectric properties appeared in the bismuthinite (Bi₂S₃)aikinite (CuPbBiS₃) series.²⁰ In this recent article, Maji et al. showed that synthetic gladite is disordered in contrast to natural gladite which is an ordered (Cu and the vacancy) structure. A high thermoelectric figure of merit zT in the range of 0.30 to 0.43 at 700 K has been achieved by tuning the carrier concentration of the gladite phase (CuPbBi₅S₉, x = 0.33) by replacing part of S with Cl.²⁰ These investigations by Liang et al. and Maji et al. reiterate the potential of finding thermoelectric materials in the bismuthinite-aikinite solid solution series and the opportunities to tune the compositions to achieve high zT. Therefore, it is important to investigate each of these Cu-deficient aikinite compositions within the solid solution series and understand the interplay between the composition and thermoelectric properties. As both recent reports are mainly focused on the gladite (x = 0.33) structure, we sought to investigate a composition close to that of pekoite (CuPbBi $_{11}S_{18}$, $x\sim0.16$) but in the disordered aikinite structure type. In this work, we have synthesized three different compositions $Cu_xPb_xBi_{2-x}S_3$ [x = 0.14(I), 0.33(II), and 1(III)] using a high-temperature solid state reaction. All the phases exhibit ultralow thermal conductivities (<0.65 W m⁻¹ K⁻¹), while a high Seebeck coefficient value and low electrical conductivity of I (x = 0.14) yielded a good zT at

moderately low temperatures. The source of low lattice thermal conductivity is further discussed in light of density functional theory (DFT)-based phonon calculations.

EXPERIMENTAL SECTION

Synthesis. Compounds I-III are derivatives of the Bi₂S₃ structure. In our synthesis, we targeted different amounts of Cu and Pb substitution for Bi in Bi₂S₃ with the nominal compositions, $Cu_{0.2}Pb_{0.2}Bi_{1.8}S_3, \quad Cu_{0.33}Pb_{0.33}Bi_{1.66}S_3, \quad \text{and} \quad CuPbBiS_3 \quad \text{for} \quad \textbf{I-III},$ respectively. The compounds, I-III, were prepared by combining stoichiometric ratios of Cu (Aldrich, 99%), Bi (Cominco Electronic Materials), Pb (Alfa Aesar, 99.9%), and S (Alfa Aesar, 99.99%) powders. The powdered elements were weighed according to the stoichiometry and filled (total weight of 3 g) into quartz ampoules (diameter = 12 mm) in an argon-filled glovebox ($O_2 < 0.1$ ppm). The loaded ampoules were taken out of the glovebox with the help of adapters and flame-sealed under vacuum. The sealed ampoules were subjected to heating at a rate of 20 °C h⁻¹ to 700 °C and held at that temperature for 4 days and then allowed to cool down at a rate of 35 °C h⁻¹ to room temperature. The cooled ampoules contained a silver ingot of the product. From broken pieces of ingots, it was possible to get a good-quality single crystal for sample I; however, for II and III, single-crystal X-ray diffraction (XRD)-quality crystals were not found. The ingots were ground into fine powder samples for the evaluation of bulk purity and further characterization.

Single-Crystal X-ray Diffraction. The single-crystal XRD-quality crystal from sample I was mounted on a Bruker Smart Apex diffractometer fitted with a Mo K α X-ray source ($\lambda = 0.71073$ Å). SMART²¹ software was used to collect data in ω swing with 20 s/frame of exposure time. The programs SAINT²² and SADABS,²² respectively, were used for data integration and absorption correction. The crystal structure was solved using SHELXS-97 from the difference Fourier map.²³ The SHELXTL-PLUS suite was used for full-matrix least-squares refinement against |F²|. SHELX-2018 embedded in SHELXLe was used for final refinements.²⁴ The crystal structure solution is in good agreement with the reported structure close to the composition of I but with a subtle difference in Bi/Pb disordered sites. The compound crystallizes in the Pnma space group (no. 62). Two heavy atoms (both assigned as Bi initially) and three S atoms all in 4c Wyckoff positions were located from the Fourier map. Upon subsequent refinements, the position of Cu was located, and an e-density slightly displaced from Bi2 also appeared. This new e-density was designated as Pb substitution (Pb1), and the occupancies of both Bi2 and Pb1 were refined independently constraining their sum of occupancies as 100%. Similarly, the occupancy of Cu was also refined. The refined occupancies, ~86% for Bi, ~14% Pb, and ~12% for Cu, remained stable in subsequent anisotropic refinements. The Cu occupancy was made to 14% for the final cycle of refinements to obtain a charge-balanced formula of $Cu_{0.14}Pb_{0.14}Bi_{1.86}S_3$, which is slightly off from the targeted composition (Cu_{0.2}Pb_{0.2}Bi_{1.8}S₃) for sample I. Such a shifted position for Pb from Bi is not totally uncommon as it has been found in the case of makovickyite.¹⁰ More importantly, we did not find any additional reflections that would indicate a larger supercell for an ordered or commensurately modulated structure. The crystallographic data containing the refinement parameters and important bond distances are listed in crystallographic Tables 1 and 2, respectively. The atomic coordinates and their isotropic and anisotropic thermal parameters are given in Tables S1 and S2, respectively.

Powder X-ray Diffraction. The bulk purity of the samples was evaluated using powder XRD (PXRD) on finely ground samples using a PANalytical X'Pert diffractometer fitted with a Cu $K\alpha$ anode over a 2θ range of 5–90°. The crystal structures and atomic coordinates of disordered aikinite structures are reported in the literature¹¹ and ICSD database for most x in Cu_xPb_xBi_{2-x}S₃ composition. To evaluate the phase purity and change in the unit cell dimensions with respect to Cu and Pb substitution, we performed Rietveld refinements of the PXRD patterns of the bulk phases and the hot-pressed samples using the atomic coordinates from the reported crystal structures, ICSD

Table 1. Crystal Data and Refinement Details for $\text{Cu}_{0.14}\text{Pb}_{0.14}\text{Bi}_{1.86}\text{S}_3$ (I) Obtained from Single-Crystal X-ray Structure Solution

empirical formula	Cu _{0.14} Pb _{0.140} Bi _{1.86} S ₃
formula weight	522.79
temperature	296(2) K
wavelength	0.71073 Å
crystal system	orthorhombic
space group	Pnma
unit cell dimensions	a = 11.358(2) Å
	b = 3.994(2) Å
	c = 11.168(3) Å
volume	506.61(4) Å ³
Z	4
density (calculated)	6.854 Mg/m^3
absorption coefficient	70.788 mm ⁻¹
goodness-of-fit on F2	1.094
$R[I > 2\sigma(I)]$	R1 = 0.0304
wR (F2) (all data)	wR2 = 0.0681

Table 2. Selected Bond Lengths (Å) for Cu_{0.14}Pb_{0.14}Bi_{1.86}S₃ (I) Obtained from Single-Crystal X-ray Structure Solution

moiety	distance (Å)	moiety	distance (Å)
Bi1-S2 ^{#1}	2.677(2)	Pb1-S1 ^{#6}	2.890(2)
Bi1-S2 ^{#2}	2.677(2)	Pb1-S1 ^{#2}	2.882(3)
Bi1-S3	2.681(3)	Pb1-S1 ^{#1}	2.882(3)
Bi1-S2 ^{#3}	3.044(3)	Pb1-S3 ^{#7}	2.934(4)
Bi1-S1 ^{#4}	3.052(2)	Pb1-S3 ^{#8}	2.934(4)
Bi1-S1 ^{#5}	3.052(2)	Cu1-S1	2.250(3)
Bi2-S1 ^{#6}	2.575(4)	Cu1-S3#8	2.356(7)
Bi2-S3 ^{#7}	2.750(3)	Cu1-S3 ^{#7}	2.356(7)
Bi2-S3 ^{#8}	2.750(3)	Cu1-S2	2.371(4)
Bi2-S1 ^{#2}	2.980(3)		
Bi2-S1 ^{#1}	2.980(3)		

"Symmetry transformations used to generate equivalent atoms: #1 -x + 1/2, -y, z + 1/2, #2 -x + 1/2, -y + 1, z + 1/2, #3 x - 1/2, y, -z + 1/2, #4 -x, -y + 1, -z + 1, #5 -x, -y, -z + 1, #6 x + 1/2, y, -z + 1/2, #7 -x + 1/2, -y, z - 1/2, #8 -x + 1/2, -y + 1, z - 1/2.

197449 ($\text{Cu}_{0.2}\text{Pb}_{0.2}\text{Bi}_{1.8}\text{S}_3$)¹¹ and 197450 ($\text{Cu}_{0.33}\text{Pb}_{0.33}\text{Bi}_{1.67}\text{S}_3$)¹¹ for compounds I and II, respectively, and ICSD 9120 (aikinite, CuPbBiS₃)¹⁷ for compound III. The refinements were performed using GSAS II software.²⁵ The calculated and the experimental patterns merged very well with acceptable values of weighted profile residuals, R_{wp} (Table 3 and Figures 1 and S1), confirming the accuracy of the model. The Rietveld-refined unit cell parameters (Table 3) are consistent with the percentage of Cu and Pb substitution in the disordered aikinite structure type for different x in $\text{Cu}_x\text{Pb}_x\text{Bi}_{2-x}\text{S}_3$ reported in the literature ^{11,17} and our single-crystal X-ray structure solution for I (compare Tables 1 and 3 for I). Note

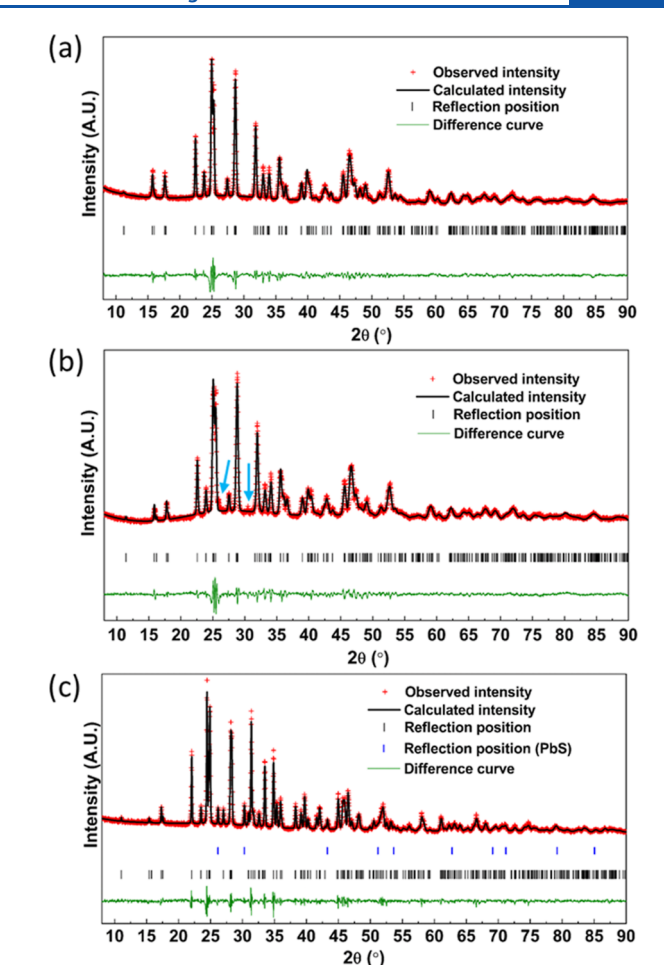


Figure 1. Rietveld refinement plots for hot-pressed samples of compounds $Cu_{0.14}Pb_{0.14}Bi_{1.86}S_3$, **I** (a), $Cu_{0.33}Pb_{0.33}Bi_{1.68}S_3$, **II** (b), and $CuPbBiS_3$, **III** (c) showing the observed, calculated, and difference curves. The arrows indicate the presence of a minute quantity of an unknown impurity phase.

that for compound I, though coordinates of $\text{Cu}_{0.2}\text{Pb}_{0.2}\text{Bi}_{1.8}\text{S}_3$ were used, the final lattice parameters and refined occupancy of Cu indicated the formula to be more close to that of our single-crystal solution for I, $\text{Cu}_{0.14}\text{Pb}_{0.14}\text{Bi}_{1.86}\text{S}_3$, whereas II and III conform to the targeted compositions of $\text{Cu}_{0.33}\text{Pb}_{0.33}\text{Bi}_{1.67}\text{S}_3$ and CuPbBiS_3 (aikinite) with Cu/vacancy and Pb/Bi disorder and the ordered aikinite structure type, respectively. However, the presence of a trace amount of the impurity phase (s) was evident in compounds II and III. The identity of the impurity phase could not be determined in case II, while in case of III, the same unknown impurity as that in II appeared along with PbS. After hot pressing, the amount of the unknown impurity decreased, but amount of PbS increased. However, energy-dispersive X-ray spectroscopy (EDS) mapping showed signs of

Table 3. Refined Lattice Constants and Rietveld Refinement Details for Pristine and Hot-Pressed Samples of I-III

	pristine	hot-pressed	pristine	hot-pressed	pristine	hot-pressed
formula	$Cu_{0.14}Pb_{0.14}Bi_{1.86}S_3$ (I)		$Cu_{0.33}Bi_{0.33}Bi_{1.68}S_3$ (II)		CuPbBiS ₃ (III)	
unit cell	11.383(2)	11.369(2)	11.444(2)	11.434(3)	11.610(3)	11.609(3)
	3.997(3)	3.994(4)	4.008(3)	4.006(3)	4.0414(2)	4.041(2)
	11.179(3)	11.171(2)	11.199(2)	11.190(2)	11.329(2)	11.343(3)
volume	508.72(2)	507.37(3)	513.76(2)	512.63(4)	531.607(8)	532.257(9)
wR (%)	3.960	5.058	6.328	5.051	4.441	3.923
RF (%)	3.403	2.874	4.802	4.606	4.922	3.743
RF^2 (%)	6.041	5.205	7.861	8.586	6.682	6.164

scattered Cu-rich phases on the surface of the pellet most likely due to the conversion of the unknown impurity into PbS and a Cu-rich phase. The Cu-rich impurity phase moves through the grain boundary to the surface during hot-pressing. Further details of Rietveld refinement are given in the Supporting Information. The refined atomic coordinates and their thermal parameters are listed in Tables S3 and S4 for as-synthesized and hot-pressed samples, respectively.

Optical Band Gap Measurements. The optical band gap of the materials was measured using a Varian Cary 5000 UV-vis-NIR spectrophotometer with mounted praying mantis mirror sets for reflectance mode measurements using BaSO₄ powder (Fisher, 99.2%) as a standard white material. Diffuse reflectance spectra were collected in the wavelength range 200–2500 nm on compounds I–III. Tauc plots (Figure 2) were generated to estimate the band gap of the

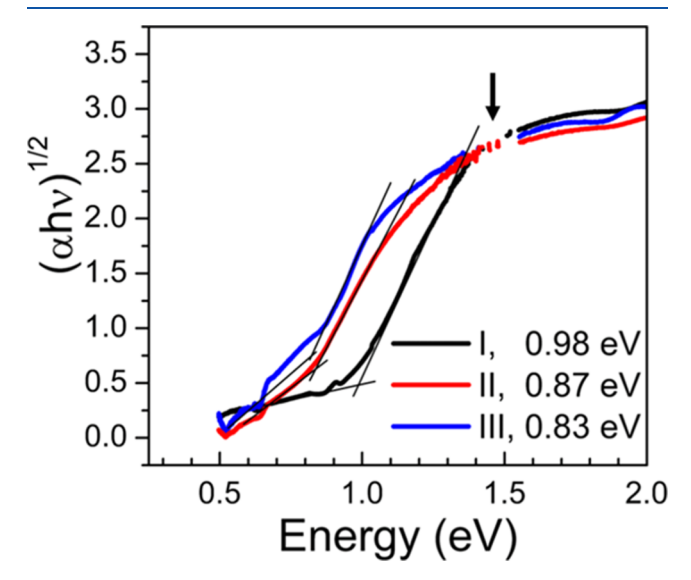


Figure 2. Diffuse reflectance spectra plotted as $h\nu$ vs $(\alpha h\nu)^{1/2}$ for compounds $\text{Cu}_{0.14}\text{Pb}_{0.14}\text{Bi}_{1.86}\text{S}_3$ (I), $\text{Cu}_{0.33}\text{Pb}_{0.33}\text{Bi}_{1.66}\text{S}_3$ (II), and CuPbBiS_3 (III). Some noisy data point in the detector change region at 1.55 eV has been removed.

materials. The optical band gaps were estimated using the equation $\alpha h \nu = A(h \nu - E_s)^m$, where α is the absorption coefficient (Kubelka–Munk function) and $h \nu$ is the photon energy. The value of m determines the direct or indirect nature of the band gap; for example, m=2 and 1/2 signify the indirect and direct gap, respectively. In the cases of compounds I–III, the $h \nu$ versus $(\alpha h \nu)^{1/2}$ plot (Figure 2) shows linearity, indicating that the compounds possess an indirect band gap. Indirect band gap values of 0.98, 0.87, and 0.83 eV were obtained for compounds I–III, respectively. A band gap of 0.87 eV for composition $Cu_{0.33}Pb_{0.33}Bi_{1.67}S_3(II)$ is in very good agreement with a band gap value of 0.89 eV reported for CuPbBi₅S₉ by Maji et al. It is evident that as the amount of Cu and Pb increases in the composition, the optical band gap decreases as observed in compounds I through III.

Sample Preparation for Transport Property Measurements. All the samples were first ground into fine powders using a mortar and pestle inside an argon-filled glovebox. Hot pressing of the powder samples was performed in a 0.5 inch-diameter graphite die under a load of 35 MPa in a highly pure argon atmosphere. Temperature was gradually increased to 500 °C, and the furnace was maintained at 500 °C for 20 min before cooling to 250 °C over 2 h duration. The load was released at 250 °C, and the cylindrical pellets were recovered after the furnace reached room temperature.

Scanning Electron Microscopy and EDS Analysis. Elemental analysis was performed on a scanning electron microscope using a TESCAN-ASCAT system fitted with a Bruker's EDS system. The elemental mapping showed even and homogeneous distribution of Cu, Pb, Bi, and S with average ratios of 0.16:0.15:1.87:3,

0.36:0.38:1.64:3, and 1.1:0.98:41.06:3 for I, II, and III, respectively, which agree very well with the added stoichiometry and X-ray-derived compositions (Figures S2–S4 and Table S5). The presence of the copper-rich impurity phase in III was evident on the surface of the polished pellet of III. However, note that in PXRD of the pressed pellet, we observed only PbS as the recognizable crystalline impurity.

Transport Properties. Thermal diffusivity $\alpha(T)$ was measured on highly polished hot-pressed pellets coated with graphite. Measurements were performed from room temperature to 475 K on compounds I–III on a NETZSCH LFA 457 MicroFlash in Davis and from 475 to 700 K on Anter FlashLine 5000 Laser Flash in Rolla under highly pure helium and argon atmospheres, respectively. Thermal conductivity, κ , was obtained by employing the relationship $\kappa = \alpha(T) \cdot C_P \cdot d$ (where $\alpha(T)$ = thermal diffusivity, C_P = specific heat, and d = density). C_P was calculated using the Dulong–Petit formula, $C_P = 3R/M$ (where R = ideal gas constant and M = average molar mass of each element), and the density of each sample was calculated from the dimension of the pellet and its mass. The measured densities were about 95% of the theoretical densities.

Bars with dimensions ${\sim}10~\text{mm}\times2~\text{mm}\times1~\text{mm}$ were cut from the hot-pressed pellets on which thermal conductivity measurements were performed in Davis. High-temperature measurements of the resistivity and Seebeck coefficient were carried out on these polished bars with a Linseis LSR-3 instrument. A standard four-probe technique was used for the measurements from 300 to 475 K under a highly pure helium atmosphere. Compounds II and III were found to be too resistive to measure electrical resistivity with this instrument. Therefore, Seebeck and electrical resistivity measurements were performed only on compound I.

Theoretical Calculations. Electronic band structure calculations were performed employing DFT as implemented in the Vienna Abinitio computational Package. $^{27-30}$ The revised Perdew–Burke– Ernzerhof (PBESol) generalized gradient approximation (GGA) was used for the density functional, and to account for the effect of core electrons, projector augmented wave pseudopotential was employed. Kinetic energy termination was set to 520 eV, and a Monkhorst-Pack³¹k-point grid size of $4 \times 6 \times 5$ was used for Brillouin zone integration. For structure optimization, a convergence threshold of 10⁻⁶ eV was set for total energy, and a maximum force of 10⁻³ eV/Å was used. All phonon calculations were performed using the code PhonTS (Phonon Transport Simulator) developed by one of the authors.32 The model of the random structure for Cu_{1-x} D_{1-x} Pb_{1-x} Bi_{1+x} S₃ compounds was prepared using a special quasi-random structure $(SQS)^{33}$ generator as implemented in the ATAT suit.³⁴ Due to the system size limitations, our model has concentrations of Cu and Pb at 12.5% (x = 0.875), very close to but not exactly 14.0% concentrations observed experimentally for compound I. We expect that this difference will not affect our conclusions.

■ RESULTS AND DISCUSSION

Structure Description. Compounds I-III can be described as disordered derivatives of Bi₂S₃, with incremental Bi + vacancy \rightarrow Pb + Cu substitution in a general formula, $Cu_{1-x} \square_x Pb_{1-x} Bi_{1+x} S_3$. To understand the crystal structure of the solid solutions, it is necessary to describe the crystal structure of one of the end members, Bi₂S₃. The crystal structure of Bi₂S₃ consists of ribbons of Bi₄S₆ with two distinct metal sites, Bi1 and Bi2. Bi1 adopts a six-coordinate distorted octahedral configuration, while the Bi2 site is five-coordinate with S atoms in square pyramid fashion, and edge sharing between these polyhedra forms ribbons of Bi₄S₆. These ribbons are stacked along the a-axis and held together through weaker Bi-S bonds with longer Bi-S distances (Bi1-S ~ 3.38 and Bi2-S \sim 3.32 Å). The inter-ribbon space is empty (a vacant site) in pure Bi_2S_3 ($Cu_{1-x}\square_x Pb_{1-x}Bi_{1+x}S_3$, x = 1). As one starts to substitute Pb²⁺ and Cu⁺ for Bi³⁺, Cu starts to fill the empty tetrahedral site in the inter-ribbon space connecting the two

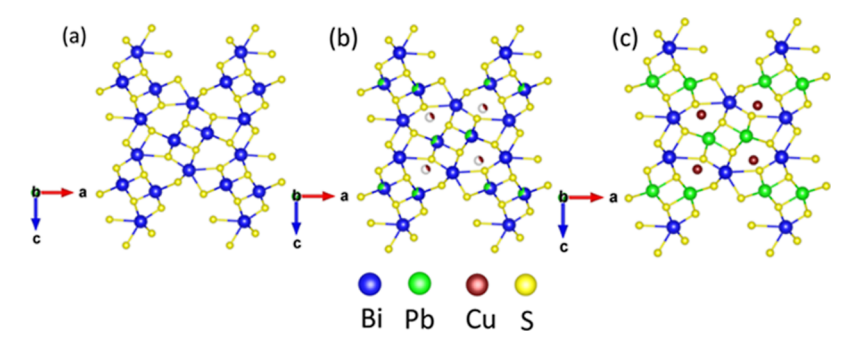


Figure 3. Framework structure showing the occupancy of Cu in tetrahedral holes and mixed occupancy of Bi2/Pb1 compared to that of the pristine Bi₂S₃ structure (a) Bi₂S₃, ICSD 171864, (b) Cu_{0.33}Pb_{0.33}Bi_{1.68}S₃, ICSD 197450 (II), (II), (a) diameter (a) Bi₂S₃ (III), ICSD 9120. (b) Cu_{0.33}Pb_{0.33}Bi_{1.68}S₃, ICSD 197450 (III), (c) CuPbBiS₃ (III), ICSD 9120. (c) CuPbBiS₃ (

individual ribbons, and Pb2+ starts to share the Bi2 site. A series of solid solutions are thus formed until Bi2 is fully replaced by Pb and Cu to form another end member, the aikinite, CuPbBiS₃. Figure 3 illustrates the structures with increasing Cu occupancy in the inter-ribbon space through replacement of Bi with Cu and Pb. Although the natural and synthetic analogues of the bismuthinite-aikinite series are compositionally similar, there exist differences in their longrange ordering. The synthetic analogues tend to form a disordered structure between Cu/vacancy and Pb/Bi compared to naturally occurring compositions, which often form superstructures due to ordering.²⁰ A similar situation was observed in the makovickyite-type compound Ag_{0.34}Bi_{4.54}Cu_{1.98}PbS₉, where the naturally occurring composition has an ordered structure, whereas the synthetic analogue displays a disordered structure. These slight structural differences are likely due to the differences in the synthesis routes. A slow natural crystal growth process often yields an ordered phase as opposed to the disordered phase often obtained in the high-temperature synthesis route used in the laboratory. From the above-mentioned discussion, it is now clear that the bismuthinite-aikinite solid solution series offers an exceptional freedom to tune the composition and band gap for the optimum thermoelectric performance.

Band Structure Analysis. Electronic band structure calculations were performed on Bi₂S₃ and CuPbBiS₃ (III) to understand the effect of Cu and Pb in modifying the states near valence and conduction bands. A calculated band gap of 1.2 eV for Bi₂S₃ is in good agreement with other reported values using the GGA functional³⁶ and slightly lower than the experimental band gap value of 1.35 eV.³⁷ The band gap of CuPbBiS₃ (III) was calculated for the first time, and the calculated band gap of 0.5 eV is slightly lower than the experimental value of 0.83 eV. As shown in Figure 4, the band structure of Bi₂S₃ has major contribution from S p states in the valence band with Bi p and S p states in the conduction band. Upon substitution with Cu and Pb, the contribution of Cu d states to the valence band becomes predominant with Bi p admixed with S p states forming the conduction band. Narrowing of the band gap upon substitution with Cu and Pb for Bi as observed from DFT calculations is also consistent with experimental band gap values calculated from diffuse reflectance spectroscopy. Strong overlap of Cu d states and S p states raises the Fermi level, thus narrowing the band gap.

Transport Properties. Figure 5 displays thermoelectric properties of compound I between room temperature and 475 K as a function of temperature and thermal conductivity data for compounds I–III between room temperature and 700 K.

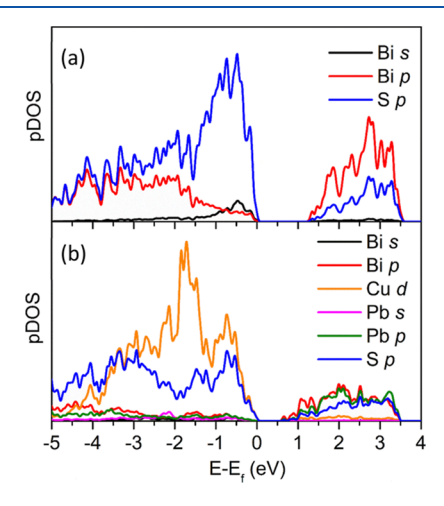


Figure 4. Partial electronic density of states (a) $\mathrm{Bi}_2\mathrm{S}_3$. Atomic coordinates are taken from ICSD 171864. (b) $\mathrm{CuPbBiS}_3$ (III). Atomic coordinates are taken from ICSD 9120. (19)

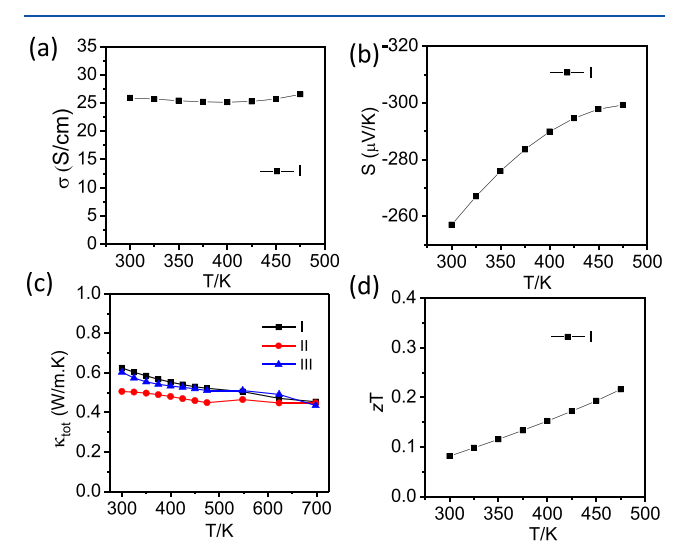


Figure 5. Temperature dependence of thermoelectric properties for compounds Cu_{0.14}Pb_{0.14}Bi_{1.86}S₃, **I**, Cu_{0.33}Pb_{0.33}Bi_{1.66}S₃, **II**, and CuPbBiS₃, **III**. (a) Electrical conductivity of **I**, (b) Seebeck coefficient of **I**, (c) thermal conductivity of **I** - **III**, and (d) figure of merit of **I**.

Compound I exhibits a room-temperature electrical conductivity of 25.9 S/cm as shown in Figure 5a. For compound I, electrical conductivity shows a sluggish change in the measured temperature range indicating degenerate semiconducting nature of the compound. However, we do notice that conductivity has a slightly increasing trend starting at 425 K,

which is also accompanied by a slight downturn in Seebeck around the same temperatures. There could be several possible reasons for this: (1) onset of bipolar conduction, ³⁸ (2) onset of Cu-ion mobility, and (3) structural or compositional change. Generally, onset of bipolar conduction is associated with a maximum in Seebeck, and the magnitude of the maximum Seebeck coefficient is related to the band gap by the Goldsmid–Sharp analytical expression, $E_{\rm g} = 2e|S|_{\rm max}T_{\rm max}^{39,40}$ According to this relation, the band gap is found to be 0.28 eV for a maximum absolute Seebeck value of 297 $\mu V K^{-1}$ at a $T_{\rm max}$ of 473 K, which is much smaller than our optical band gap (\sim 0.9 eV). Therefore, it is unlikely to have an onset of bipolar conduction at 425 K; with a band gap of \sim 0.9 eV, the bipolar conduction is expected at much higher temperature (\sim 850 K). From the single-crystal structure solution, the position of the Cu ion is found to be very well-behaved. Also, with the onset of Cu ion mobility, one would observe a change in thermal conductivity, which is not the case here. Therefore, it does not seem to support Cu-ion mobility as a reasonable possibility. Our thermogravimetry-DSC experiment on sample I indicates the absence of any structural changes before the melting; however, a slight weight loss (~0.13%) presumably due to sulfur loss is observed (Figure S5). It is possible that the sulfur vacancy may be contributing to the improvement of conductivity at that temperature. As shown in Figure 5b, very large negative Seebeck coefficient values are observed for compound I, implying electrons as the major charge carriers. The Seebeck coefficient of compound I is 257 μ V K⁻¹ at 300 K and gradually increased to 297 μ V K⁻¹ at 475 K. Recently reported TE properties on compound CuPbBi₅S₉, ²⁰ which is isostructural to compound II, have a very low electrical conductivity of 2.85×10^{-4} S/cm and a very large negative Seebeck coefficient value, $S = -1370 \,\mu\text{V K}^{-1}$, at 375 K due to a very small carrier concentration. However, for similar composition, Liang et al. reported a range of Seebeck coefficients and electrical conductivity values, highly dependent on the mode of synthesis adapted. 19 These differences could arise due to slight nonstoichiometry in the composition and the subsequent presence of various numbers of defects. Hence, it is now clear that highly resistive nature of compounds II and III may have resulted from a very low charge carrier concentration indicative of charge-balanced compositions. In compound I, the large Seebeck coefficient is consistent with the low electrical conductivity value, indicative of the low concentration of charge carriers. The power factors vary between 1.71 and 2.37 μ W cm⁻¹ K⁻² for compound I in the temperature range 300-475 K (Figure 6a).

Figure 5c depicts the plot of $\kappa_{\rm tot}$ in the temperature range 300–700 K for compounds I–III. The compounds I–III display ultralow thermal conductivity with values in the range

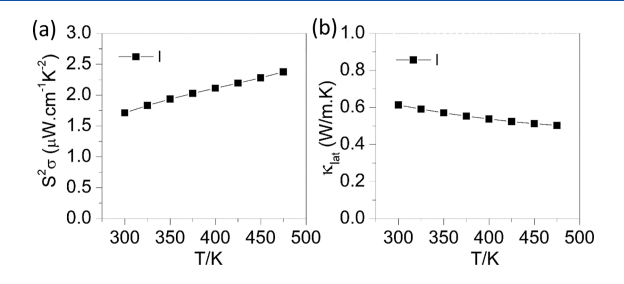


Figure 6. (a) Power factors and (b) lattice thermal conductivity (κ_{lat}) for $Cu_{0.14}Pb_{0.14}Bi_{1.86}S_3$, **I**, from 300 to 475 K.

of 0.45-0.62 W m⁻¹ K⁻¹. The thermal conductivity values at room temperature (300 K) do not vary much for the three compounds, and they are 0.62, 0.5, and 0.6 W m^{-1} K⁻¹, respectively, for I, II, and III. These values also corroborate those reported by Liang et al. (0.44 W m⁻¹ K⁻¹ at 298 K)¹⁹ and Maji et al. (0.59 W m⁻¹ K⁻¹ at 300 K)²⁰ for pristine CuPbBi₅S₉ and reiterate that small percentages of PbS/ unknown impurities in II and III do not impact the intrinsic thermal conductivity of the materials. These values are also comparable to those of many low-thermal conductivity complex chalcogenide-based systems, for example, 0.6 W m^{-1} K⁻¹ in AgBi₃S₅, 41 0.67–1.00 W m^{-1} K⁻¹ in MBi₄S₇ (M = Mn, Fe), 42 and 0.61 W m^{-1} K⁻¹ in the makovickyite-type compound, Ag_{0.34}Bi_{4.54}Cu_{1.98}PbS₉. 10 The electronic contribution can be separated from the total thermal conductivity by employing the Wiedemann–Franz law, $\kappa_{\rm ele}$ = $L\sigma T$, where L is the Lorenz number. L is related to the Seebeck coefficient through the equation L = 1.5 + exp $\left[\frac{-|\mathbf{S}|}{116}\right]$ where the value of Lis given in 10^{-8} W Ω K⁻² and S is in μ V K⁻¹. Lattice thermal conductivity, κ_{lat} can be obtained by deducting the electronic part from the total thermal conductivity ($\kappa_{tot} = \kappa_{ele} + \kappa_{lat}$). The lattice thermal conductivity, $\kappa_{lat} = 0.61 \text{ W m}^{-1} \text{ K}^{-1}$, for compound I is very close to a κ_{tot} value of 0.62 W m⁻¹ K⁻¹ at room temperature. The very little electronic contribution is in agreement with the low electrical conductivities (Figure 6b).

Low thermal conductivity in some members of this family of compounds was explained in the literature based on the "rattler" atoms represented by the Cu atoms. 43 Associated with the rattler atoms are the low-energy optical phonon modes that efficiently scatter the acoustic phonons and effectively reduce the thermal conductivity. To verify if the same mechanism is responsible for observed thermal conductivity in our compounds, we carried out phonon density of states (PDOS) and projected PDOS calculations for compound I that features random distribution of Cu and Pb atoms. To model this random distribution, we utilized SQS structures that permit simulating random atomic distributions based on the relatively small supercells. Here, the smallest possible cell contains 8 primitive cells, which correspond to 164 atoms in the cell (4Cu, 4Pb, 60Bi, and 96S) giving the required composition. The SQS structure was generated, fully relaxed, and we carried out PDOS calculations. The resultant PDOS is presented in Figure 7. We show both total density of states and projected density of states for the individual atom types. Our PDOS agrees very well with that presented by Maji et al.²⁰ for aikinite CuPbBiS3, indicating similar influence of Cu on the phonon properties of these compounds. This is even though aikinite is an ordered compound, while we consider disordered Cu_{0.125}Pb_{0.125}Bi_{1.875}S₃. One can clearly see that while Cu atoms have non-negligible contribution to the PDOS at low frequencies, most of their contribution is in the mid-frequency region, well above the acoustic mode peak. We thus conclude that it is unlikely that rattler modes are responsible for the lowering of the thermal conductivity; rather, the random structure of the compound is responsible for this behavior.

It needs to be pointed out here that the room-temperature thermal conductivity of compounds I-III is 2 to 3 times lower than that of the bulk Bi_2S_3 compound.³⁷ Among compounds I-III, compound II has intermediate composition between compounds I and III but showed the lowest thermal conductivity of 0.5 W m⁻¹ K⁻¹ at room temperature. It is clear that the lattice thermal conductivity is drastically

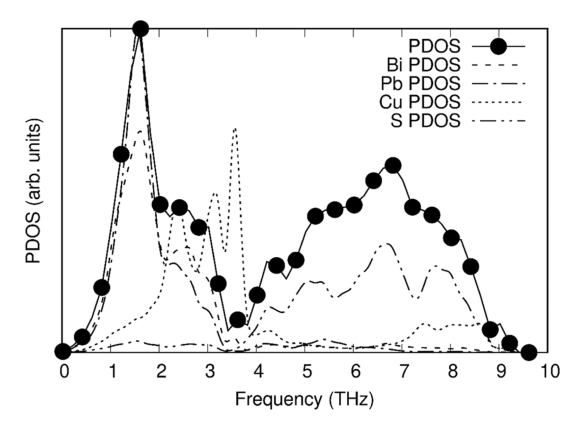


Figure 7. Phonon DOS and projected into the individual atom PDOS of the model compound ($Cu_{0.125}Pb_{0.125}Bi_{1.875}S_3$). Note phonon modes to which copper atoms make the most contribution to (dashed–dotted line): ~2 to 4 THz, well above the acoustic phonon peak of 1.5 THz.

suppressed by introducing Cu and Pb in the structure; however, there may be an optimum Cu/vacancy ratio to display lowest thermal conductivity since further increase in the amount of Cu and Pb did not show a significant change. These insights will help in optimizing the electrical properties without affecting the low lattice thermal conductivity.

Low thermal conductivity and large Seebeck coefficient values coupled with low electrical conductivity produced a promising zT of 0.21 at 475 K for compound I (Figure 5d). Note that Maji et al. reported a zT value of 0.04 at 700 K for pristine CuPbBi₅S₉, which was further increased to 0.43 upon Cl doping. However, in this work, a zT value of 0.21 has been achieved at a moderate temperature of 475 K without any additional doping. Higher zT of compound I compared to that of other members in the series could be the result of intrinsic non-stoichiometry in the composition. This non-stoichiometric effect contributes to the higher carrier concentration which results in moderately higher zT. Hence, compound I, $Cu_{0.14}Pb_{0.14}Bi_{1.86}S_3$, would be an ideal candidate for further aliovalent doping to increase the carrier concentration which will ultimately increase zT.

CONCLUSIONS

Three quaternary complex chalcogenides, $Cu_xPb_xBi_{2-x}S_3$ (x=0.14(I), 0.33(II), and 1(III)), are successfully synthesized in the bismuthinite—aikinite solid solution series. These compounds are narrow-band gap indirect n-type semiconductors with band gaps in the range of 0.8-1.0 eV. Ultralow thermal conductivities less than $0.65~W~m^{-1}~K^{-1}$ are 2 to 3 times lower than those of the pristine Bi_2S_3 compound suggesting the critical role of the interstitial Cu ions and stereochemical lone pairs on Pb in suppressing the lattice thermal conductivity; however, we eliminate the rattling of Cu atoms as a possible mechanism. A promising zT of 0.21 at 475 K for compound I warrants further investigation to tune the thermoelectric properties especially in increasing the electrical conductivity through monovalent anion doping.

ASSOCIATED CONTENT

Supporting Information

The Supporting Information is available free of charge at https://pubs.acs.org/doi/10.1021/acsaem.2c02790.

Crystallographic information (CIF) file for the single-crystal X-ray structure solution of I (CSD number: 2203924); single-crystal atomic coordinate, isotropic, and anisotropic thermal parameters; Rietveld refined atomic coordinates and isotropic thermal parameters of as-synthesized and hot-pressed samples of I–III; atomic percentage of elements from EDS analysis; PXRD patterns from Rietveld refined data of as-synthesized samples; and EDS mapping of the elements in the hot-pressed pellets (PDF)

Single-crystal X-ray structure solution of I (CIF)

AUTHOR INFORMATION

Corresponding Author

Amitava Choudhury — Department of Chemistry, Missouri University of Science and Technology, Rolla, Missouri 65409, United States; orcid.org/0000-0001-5496-7346; Email: choudhurya@mst.edu

Authors

Srikanth Balijapelly — Department of Chemistry, Missouri University of Science and Technology, Rolla, Missouri 65409, United States; Occid.org/0000-0003-2720-8568

Ashlee Hauble — Department of Chemistry, University of California, Davis, California 95616, United States;
orcid.org/0000-0002-2794-9916

Santhoshkumar Sundaramoorthy – Department of Chemistry, Missouri University of Science and Technology, Rolla, Missouri 65409, United States; orcid.org/0000-0001-5037-0016

Jeremy Lee Watts – Department of Materials Science and Engineering, Missouri University of Science and Technology, Rolla, Missouri 65409, United States; ocid.org/0000-0002-4150-5254

Susan M. Kauzlarich — Department of Chemistry, University of California, Davis, California 95616, United States;
orcid.org/0000-0002-3627-237X

Aleksandr Chernatynskiy — Department of Physics, Missouri University of Science and Technology, Rolla, Missouri 65409, United States; orcid.org/0000-0001-7431-7201

Complete contact information is available at: https://pubs.acs.org/10.1021/acsaem.2c02790

Author Contributions

The problem was conceived and supervised by A.C. Synthesis, characterization of samples, preparation of pellets, band gap measurements, and the band structure calculations were performed by S.B. S.S. repeated some of the characterization in the revised version. A.H. and S.M.K. contributed to high-temperature TE measurements. A.V.C. performed phonon density calculations. J.L.W. assisted in hot-pressing and performed high-temperature TC measurements. The initial draft of the manuscript was prepared by S.B., and all the authors contributed with their valuable inputs and approved the final manuscript.

Notes

The authors declare no competing financial interest.

ACKNOWLEDGMENTS

A.C., A.V.C., and S.B. acknowledge the National Science Foundation (NSF) under grant no DMR-1809128 for the funding of this work. Support from the NSF (DMR-201156) is

also acknowledged by A.H. and S.M.K. for this work. A.H. also thanks the NSF for her graduate fellowship.

REFERENCES

- (1) Snyder, G. J.; Toberer, E. S. Complex Thermoelectric Materials. *Nat. Mater.* **2008**, *7*, 105–114.
- (2) Shi, X. L.; Zou, J.; Chen, Z. G. Advanced Thermoelectric Design: From Materials and Structures to Devices. *Chem. Rev.* **2020**, *120*, 7399–7515.
- (3) Terasaki, I.Thermal Conductivity and Thermoelectric Power of Semiconductors. *Comprehensive Semiconductor Science and Technology*; Elsevier, 2011; Vol. 1, pp 326–358.
- (4) Rowe, D. M.CRC Handbook of Thermoelectric; CRC Press, 2018; p 182.
- (5) Ohta, M.; Chung, D. Y.; Kunii, M.; Kanatzidis, M. G. Low Lattice Thermal Conductivity in Pb5Bi6Se14, Pb3Bi2S6, and PbBi2S4: Promising Thermoelectric Materials in the Cannizzarite, Lillianite, and Galenobismuthite Homologous Series. *J. Mater. Chem.* A 2014, 2, 20048–20058.
- (6) Olvera, A.; Shi, G.; Djieutedjeu, H.; Page, A.; Uher, C.; Kioupakis, E.; Poudeu, P. F. P. Pb₇Bi₄Se₁₃: A Lillianite Homologue with Promising Thermoelectric Properties. *Inorg. Chem.* **2015**, *54*, 746–755.
- (7) Casamento, J.; Lopez, J. S.; Moroz, N. A.; Olvera, A.; Djieutedjeu, H.; Page, A.; Uher, C.; Poudeu, P. F. P. Crystal Structure and Thermoelectric Properties of the 7,7L Lillianite Homologue Pb6Bi2Se9. *Inorg. Chem.* **2017**, *56*, 261–268.
- (8) Zhao, J.; Hao, S. Q.; Islam, S. M.; Chen, H. J.; Tan, G. J.; Ma, S. L.; Wolverton, C.; Kanatzidis, M. G. Six Quaternary Chalcogenides of the Pavonite Homologous Series with Ultralow Lattice Thermal Conductivity. *Chem. Mater.* **2019**, *31*, 3430–3439.
- (9) Qu, S. Q.; Zhao, J.; Jiang, Z. M.; Jiang, D. Q.; Wang, Y. G. Pavonite Homologues as Potential n-Type Thermoelectric Materials: Crystal Structure and Performance. *Mater. Chem. Front.* **2021**, *5*, 1283–1294.
- (10) Balijapelly, S.; Hauble, A.; Pollard, M.; Poupon, M.; Petříček, V.; Watts, J. L.; Hor, Y. S.; Kauzlarich, S. M.; Choudhury, A. Ultralow Thermal Conductivity Through the Interplay of Composition and Disorder Between Thick and Thin Layers of Makovickyite Structure. *J. Mater. Chem. C* **2021**, *9*, 11207–11215.
- (11) Mumme, W. G.; Watts, J. A. P. CuPbBi11S18, A New Member of the Bismuthinite-Aikinite Mineral Series: Its Crystal Structure and Relationship with Naturally- and Synthetically-Formed Members. *Can. Mineral.* 1976, 14, 322–333.
- (12) Syněcek, V.; Hybler, J. The Crystal Structure of Krupkaite, CuPbBi3S6, and of Gladite, CuPbBi5S9, and the Classification of Superstructures in the Bismuthinite—Aikinite Group. *Neues Jahrb. Mineral., Monatsh.* 1974, 541–560.
- (13) Kohatsu, I.; Wuensch, B. J. The Crystal Structure of Gladite, PbCuBi₅S₉, a Superstructure Intermediate in the Series Bi_2S_3 -PbCuBiS₃ (Bismuthinite-Aikinite). *Acta Crystallogr., Sect. B: Struct. Crystallogr. Cryst. Chem.* **1976**, 32, 2401–2409.
- (14) Horruchi, H.; Wuensch, B. J. The Ordering Scheme for Metal Atoms in the Crystal Structure of Hammarite, Cu2Pb2Bi4S9. *Can. Mineral.* **1976**, *14*, 536–539.
- (15) Topa, D.; Balic-Zunic, T.; Makovicky, E. The Crystal Structure of Cu_{1.6}Pb_{1.6}Bi_{6.4}S₁₂, a New 44.8 Å Derivative of the Bismuthinite-Aikinite Solid-Solution Series. *Can. Mineral.* **2000**, *38*, 611–616.
- (16) Petricek, V.; Makovicky, E. Interpretation of Selected Structures of the Bismuthinite Aikinite Series as Commensurately Modulated Structures. *Can. Mineral.* **2006**, *44*, 189–206.
- (17) Kohatsu, I.; Wuensch, B. J. The Crystal Structure of Aikinite, PbCuBiS3. *Acta Crystallogr., Sect. B: Struct. Crystallogr. Cryst. Chem.* 1971, 27, 1245–1252.
- (18) Ohmasa, M.; Nowacki, W. A redetermination of the crystal structure of aikinite [BiS2lSlCuIVPbVII]*. Z. Kristallogr. 1970, 132, 71–86.

- (19) Liang, H.; Guo, J.; Zhou, Y. X.; Wang, Z. Y.; Feng, J.; Ge, Z. H. CuPbBiSS9 Thermoelectric Material with an Intrinsic Low Thermal Conductivity: Synthesis and Properties. *J. Mater.* **2022**, *8*, 174–183.
- (20) Maji, K.; Lemoine, P.; Renaud, A.; Zhang, B.; Zhou, X.; Carnevali, V.; Candolfi, C.; Raveau, B.; Al Rahal Al Orabi, R.; Fornari, R.; Vaqueiro, M.; Pasturel, P.; Prestipino, M.; Guilmeau, C.; Guilmeau, E. A Tunable Structural Family with Ultralow Thermal Conductivity: Copper-Deficient $Cu_{1-x\square x}Pb_{1-x}Bi_{1+x}S_3$. *J. Am. Chem. Soc.* **2022**, *144*, 1846–1860.
- (21) Bruker-SMART; Bruker AXS Inc.: Madison, Wisconsin, USA, 2002.
- (22) Bruker-SAINT and SADABS, and SHELXTL; Bruker AXS Inc.: Madison, Wisconsin, USA, 2008.
- (23) Sheldrick, G. M. A short history of SHELX. Acta Crystallogr., Sect. A: Found. Crystallogr. 2008, 64, 112–122.
- (24) Hübschle, C. B., Sheldrick, G. M., Dittrich, B. ShelXle: a Qt graphical user interface for SHELXL. J. Appl. Crystallogr. 2011, 44, 1281–1284.
- (25) Toby, B. H.; Von Dreele, R. B. GSAS-II: The Genesis of a Modern Open-Source All-Purpose Crystallography Software Package. *J. Appl. Crystallogr.* **2013**, *46*, 544–549.
- (26) Kubelka, P.; Munk, F. Ein Beitrag Zur Optik Der Farbanstriche. Z. Tech. Phys. 1931, 12, 593–601.
- (27) Kresse, G.; Hafner, J. Ab Initio Molecular Dynamics for Liquid Metals. *Phys. Rev. B: Condens. Matter Mater. Phys.* **1993**, 47, 558–561.
- (28) Kresse, G.; Furthmüller, J. Efficiency of ab-Initio Total Energy Calculations for Metals and Semiconductors Using A Plane-Wave Basis Set. *Comput. Mater. Sci.* **1996**, *6*, 15–50.
- (29) Kresse, G.; Furthmüller, J. Efficient Iterative Schemes for ab Initio Total-Energy Calculations Using A Plane-Wave Basis Set. *Phys. Rev. B: Condens. Matter Mater. Phys.* **1996**, *54*, 11169–11186.
- (30) Kresse, D.; Joubert, D. From ultrasoft pseudopotentials to the projector augmented-wave method. *Phys. Rev. B: Condens. Matter Mater. Phys.* **1999**, *59*, 1758–1775.
- (31) Monkhorst, H. J.; Pack, J. D. Special points for Brillouin-zone integrations. *Phys. Rev. B: Condens. Matter Mater. Phys.* **1976**, 13, 5188–5192.
- (32) Chernatynskiy, A.; Phillpot, S. R. Phonon Transport Simulator (PhonTS). *Comput. Phys. Commun.* **2015**, *192*, 196–204.
- (33) Zunger, A.; Wei, S.; Ferreira, L. G.; Bernard, J. E. Special Quasirandom Structures. *Phys. Rev. Lett.* **1990**, *65*, 353–356.
- (34) van de Walle, A.; Asta, M.; Ceder, G. The Alloy Theoretic Automated Toolkit: A User Guide. *Calphad* **2002**, *26*, 539–553.
- (35) Kyono, A.; Kimata, M. Structural Variations Induced by Difference of the Inert Pair Effect in the Stibnite-Bismuthinite Solid Solution Series (Sb, Bi)2S3. *Am. Mineral.* **2004**, *89*, 932–940.
- (36) Larson, P.; Greanya, V. A.; Tonjes, W. C.; Liu, R.; Mahanti, S. D.; Olson, C. G. Electronic Structure of Bi_2X_3 (X = S, Se, T) Compounds: Comparison of Theoretical Calculations with Photoemission Studies. *Phys. Rev. B: Condens. Matter Mater. Phys.* **2002**, 65, 085108.
- (37) Biswas, K.; Zhao, L. D.; Kanatzidis, M. G. Tellurium-Free Thermoelectric: The Anisotropic n -Type Semiconductor Bi_2S_3 . *Adv. Energy Mater.* **2012**, *2*, 634–638.
- (38) Zevalkink, A.; Smiadak, D. M.; Blackburn, J. L.; Ferguson, A. J.; Chabinyc, M. L.; Delaire, O.; Wang, J.; Kovnir, K.; Martin, J.; Schelhas, L. T.; Sparks, T. D.; Kang, S. D.; Dylla, M. T.; Snyder, G. J.; Ortiz, B. R.; Toberer, E. S. A Practical Field Guide to Thermoelectrics: Fundamentals, Synthesis, and Characterization. *Appl. Phys. Rev.* 2018, 5, 021303.
- (39) Goldsmid, H. J.; Sharp, J. W. Estimation of the Thermal Band Gap of A Semiconductor From Seebeck Measurements. *J. Electron. Mater.* **1999**, 28, 869–872.
- (40) Gibbs, Z. M.; Kim, H.-S.; Wang, H.; Snyder, G. J. Band Gap Estimation from Temperature Dependent Seebeck Measurement Deviations from the 2elSlmaxTmax Relation. *Appl. Phys. Lett.* **2015**, 106, 022112.
- (41) Tan, G.; Hao, S.; Zhao, J.; Wolverton, C.; Kanatzidis, M. G. High Thermoelectric Performance in Electron-Doped AgBi3SS with

Ultralow Thermal Conductivity. J. Am. Chem. Soc. 2017, 139, 6467-6473.

- (42) Labégorre, J. B.; Virfeu, A.; Bourhim, A.; Willeman, H.; Barbier, T.; Appert, F.; Juraszek, J.; Malaman, B.; Huguenot, A.; Gautier, R.; Nassif, V.; Lemoine, P.; Prestipino, C.; Elkaim, E.; Pautrot-d'Alençon, L.; Le Mercier, T.; Maignan, A.; Al Rahal Al Orabi, R.; Guilmeau, E. XBi₄S₇ (X = Mn, Fe): New Cost-Efficient Layered n-Type Thermoelectric Sulfides with Ultralow Thermal Conductivity. Adv. Funct. Mater. 2019, 29, 1904112-1904124.
- (43) Bhui, A.; Dutta, M.; Mukherjee, M.; Rana, K. S.; Singh, A. K.; Soni, A.; Biswas, K. Ultralow Thermal Conductivity in Earth-Abundant Cu1.6Bi4.8S8: Anharmonic Rattling of Interstitial Cu. Chem. Mater. 2021, 33, 2993-3001.

Recommended by ACS

Electronic Structure- and Entropy-Driven Design of Thermoelectric Chalcogenide Cu₅Sn₂Se₇ Leading to the Optimization of Carrier Concentration and Reduction in...

Chao Yang, Jiaolin Cui, et al.

MAY 01, 2023

ACS APPLIED ENERGY MATERIALS

READ

Synthesis and Characterization of a Trigonal Layered Compound AgInS,

Takahiro Sawahara, Yoshikazu Mizuguchi, et al.

MARCH 16, 2023

ACS OMEGA

READ

Entropy Engineering in Tellurium-Free Thermoelectric Cu₈GeSe₆ with a Stable Cubic Structure

Wen Wang, Xiaoyuan Zhou, et al.

DECEMBER 29, 2022

ACS APPLIED ENERGY MATERIALS

READ 2

High Thermoelectric Performance and Oxidation Resistance of (Na, Ga) Codoped β-Zn₄Sb₃ Thermoelectric Materials Prepared by the NaCl Flux

Jie Zheng, Shukang Deng, et al.

FEBRUARY 27, 2023

CRYSTAL GROWTH & DESIGN

READ

Get More Suggestions >